

# The discovery of radio halos in the frontier fields clusters Abell S1063 and Abell 370

C. Xie<sup>1</sup>, R. J. van Weeren<sup>1</sup>, L. Lovisari<sup>2</sup>, F. Andrade-Santos<sup>2</sup>, A. Botteon<sup>1,3</sup>, M. Brüggen<sup>4</sup>, E. Bulbul<sup>2</sup>, E. Churazov<sup>5,6</sup>, T. E. Clarke<sup>7</sup>, W. R. Forman<sup>2</sup>, H. T. Intema<sup>8,1</sup>, C. Jones<sup>2</sup>, R. P. Kraft<sup>2</sup>, D. V. Lal<sup>9</sup>, T. Mroczkowski<sup>10</sup>, and A. Zitrin<sup>11</sup>

<sup>1</sup> Leiden Observatory, Leiden University, PO Box 9513, 2300 RA Leiden, The Netherlands

e-mail: [xie@strw.leidenuniv.nl](mailto:xie@strw.leidenuniv.nl), [rvweeren@strw.leidenuniv.nl](mailto:rvweeren@strw.leidenuniv.nl)

<sup>2</sup> Center for Astrophysics | Harvard & Smithsonian, 60 Garden Street, Cambridge, MA 02138, USA

<sup>3</sup> INAF – IRA, via P. Gobetti 101, 40129 Bologna, Italy

<sup>4</sup> Hamburger Sternwarte, University of Hamburg, Gojenbergsweg 112, 21029 Hamburg, Germany

<sup>5</sup> Max Planck Institute for Astrophysics, Karl-Schwarzschild-Str 1, 85741 Garching, Germany

<sup>6</sup> Space Research Institute (IKI), Profsoyuznaya 84/32, Moscow 117997, Russia

<sup>7</sup> Naval Research Laboratory, 4555 Overlook Avenue SW, Code 7213, Washington, DC 20375, USA

<sup>8</sup> International Centre for Radio Astronomy Research – Curtin University, GPO Box U1987, Perth, WA 6845, Australia

<sup>9</sup> National Centre for Radio Astrophysics – Tata Institute of Fundamental Research, Post Box 3, Ganeshkhind PO, Pune 411007, India

<sup>10</sup> European Southern Observatory (ESO), Karl-Schwarzschild-Str. 2, 85748 Garching, Germany

<sup>11</sup> Physics Department, Ben-Gurion University of the Negev, PO Box 653, Beer-Sheva 8410501, Israel

Received 18 October 2019 / Accepted 4 February 2020

## ABSTRACT

**Context.** Massive merging galaxy clusters often host diffuse megaparsec-scale radio synchrotron emission. This emission originates from relativistic electrons in the ionized intracluster medium. An important question is how these synchrotron emitting relativistic electrons are accelerated.

**Aims.** Our aim is to search for diffuse emission in the Frontier Fields clusters Abell S1063 and Abell 370 and characterize its properties. While these clusters are very massive and well studied at some other wavelengths, no diffuse emission has been reported for these clusters so far.

**Methods.** We obtained 325 MHz Giant Metrewave Radio Telescope (GMRT) and 1–4 GHz Jansky Very Large Array (VLA) observations of Abell S1063 and Abell 370. We complement these data with *Chandra* and *XMM-Newton* X-ray observations.

**Results.** In our sensitive images, we discover radio halos in both clusters. In Abell S1063, a giant radio halo is found with a size of  $\sim 1.2$  Mpc. The integrated spectral index between 325 MHz and 1.5 GHz is  $-0.94 \pm 0.08$  and it steepens to  $-1.77 \pm 0.20$  between 1.5 and 3.0 GHz. This spectral steepening provides support for the turbulent reacceleration model for radio halo formation. Abell 370 hosts a faint radio halo mostly centered on the southern part of this binary merging cluster, with a size of  $\sim 500$ –700 kpc. The spectral index between 325 MHz and 1.5 GHz is  $-1.10 \pm 0.09$ . Both radio halos follow the known scaling relation between the cluster mass proxy  $Y_{500}$  and radio power, which is consistent with the idea that they are related to ongoing cluster merger events.

**Key words.** galaxies: clusters: individual: Abell S1063 – galaxies: clusters: individual: Abell 370 – galaxies: clusters: intracluster medium – radiation mechanisms: non-thermal

## 1. Introduction

Diffuse radio sources in galaxy clusters trace large-scale magnetic fields and relativistic electrons in the intracluster medium (ICM). Unlike the synchrotron emission from radio galaxies, diffuse cluster radio sources do not directly associate with any individual sources in the cluster. Diffuse radio sources are commonly divided into the following three different classes: radio halos, radio minihalos, and radio shocks (see, e.g., Feretti et al. 2012, Brunetti & Jones 2014, and van Weeren et al. 2019 for reviews). Radio shocks (also called relics) are elongated, arc-like objects located in the periphery of merging clusters (e.g., Venturi et al. 2007; Bonafede et al. 2009; van Weeren et al. 2009, 2016a). On the other hand, radio halos and minihalos are located at the center of the cluster with more roundish morphologies (e.g., Giovannini et al. 1993; Sijbring & de Bruyn 1998;

Brown & Rudnick 2011; van Weeren et al. 2014; Kale et al. 2015; Cuciti et al. 2018; Giacintucci et al. 2019).

Radio halos have typical sizes of  $\sim 1$  Mpc. The spectral indices<sup>1</sup> of radio halos are steep, ranging from about  $-1$  to  $-2$ . Radio halos approximately follow the X-ray emission from the hot ICM (e.g., Govoni et al. 2004), indicating a connection between the thermal and nonthermal components of the ICM. This connection is also supported by the correlation between the radio power and X-ray luminosity or cluster mass (e.g., Liang et al. 2000; Cassano et al. 2006, 2013; Basu 2012). So far, most megaparsec-size radio halos have been found in dynamically disturbed clusters, suggesting a connection between mergers and radio halo formation (e.g., Cassano et al. 2010).

<sup>1</sup> The spectral index  $\alpha$  is defined as  $F_\nu \propto \nu^\alpha$ .

There are two main models to explain the origin of radio halos. The turbulent reacceleration model proposes that the cosmic-ray (CR) electrons are reaccelerated by the turbulence induced by a cluster merging event (Brunetti et al. 2001; Petrosian 2001). In the hadronic model for radio halos, the relativistic electrons are secondary products produced by proton-proton collisions (Dennison 1980; Blasi & Colafrancesco 1999). Such collisions also produce  $\gamma$ -ray emission. Recent *Fermi*-LAT observations gave important constraints on the energy content of CR protons in clusters (Ackermann et al. 2014, 2016; Brunetti et al. 2017), which disfavor the hadronic model. The discovery of ultra-steep spectrum radio halos (i.e.,  $\alpha < -1.6$ ; Brunetti et al. 2008) has also provided support for the turbulent reacceleration model. Despite these findings, our understanding of the turbulent reacceleration mechanism remains limited.

Radio minihalos have typical sizes of  $\lesssim 500$  kpc (e.g., Feretti et al. 2012; Giacintucci et al. 2017). The most prominent difference with giant radio halos is that minihalos are not associated with merging clusters but with relaxed, cool-core clusters. Such clusters often contain a radio-loud active galactic nucleus (AGN) at their center. However, the radiative lifetime of the CR electrons from radio minihalos is too short for these electrons to have directly come from the central AGN. Therefore in-situ particle (re-)acceleration in the ICM is required to explain the existence of minihalos.

Radio minihalos have been explained by turbulent reacceleration from gas sloshing in the cluster core (Mazzotta & Giacintucci 2008; ZuHone et al. 2013). However, hadronic scenarios have also been proposed (e.g., Pfrommer & Enßlin 2004; Fujita et al. 2007; Keshet & Loeb 2010; Fujita & Ohira 2013). Although minihalos are sometimes considered as smaller versions of giant halos, the connection between halos and minihalo is still unclear (Savini et al. 2019; van Weeren et al. 2019; Kale et al. 2019).

In this paper, we present new 325 MHz Giant Metrewave Radio Telescope (GMRT) and 1–4 GHz *Jansky Very Large Array* (VLA) observations of two Frontier Fields clusters, Abell S1063 and Abell 370. Deep VLA observations of the Frontier Fields cluster MACS J0717.5+3745 and Abell 2744 were already presented in van Weeren et al. (2016b, 2017) and Pearce et al. (2017). The observations and data reduction are described in Sect. 2. In Sect. 3, we present our results and radio spectral measurements. We end with a discussion and conclusions in Sects. 4 and 5. Below we introduce these clusters in some more detail.

Throughout the paper, we adopt the flat  $\Lambda$ CDM cosmology with  $\Omega_\Lambda = 0.70$ ,  $\Omega_M = 0.30$ , and  $H_0 = 70 \text{ km s}^{-1} \text{ Mpc}^{-1}$ . At the redshifts of Abell 370 and Abell S1063, 1'' corresponds to scales of about 5.2 kpc and 4.9 kpc, respectively.

**Abell S1063 and Abell 370.** Abell S1063 (also known as RXC J2248.7–4431 or MACS 2248.7-4431, hereafter AS1063) is a massive galaxy cluster ( $z = 0.3461$ ) with a Sunyaev-Zel'dovich (SZ) derived mass of  $M_{500} \sim 1.4 \times 10^{15} M_\odot$  (Abell et al. 1989; Planck Collaboration XVII 2016; Lotz et al. 2017), see Table 1. The cluster's X-ray luminosity is  $1.8 \times 10^{45} \text{ erg s}^{-1}$  in the 0.5–2.0 keV band (Williamson et al. 2011) and the mean temperature is around 12 keV within a 800 kpc radius, which makes it one of the hottest clusters known (Gómez et al. 2012).

An observed offset between the galaxy isodensity distribution and hot gas, high X-ray temperature, and non-Gaussian galaxy velocity distribution suggest an ongoing major merger event (Gómez et al. 2012). A subsequent weak lensing study provided further support for the conclusion of an ongoing merger (Gruen et al. 2013). However, from *XMM-Newton* observations,

the high concentration value, low power ratio, and low centroid shift of the X-ray emission lead Lovisari et al. (2017) to suggest a relaxed dynamical state. It should be noted that these parameters may lead to wrong conclusions if the mergers happen along the line of sight or with a small offset.

Abell 370 (hereafter, A370) is renowned for being a strong lensing cluster ( $z = 0.375$ ) with a mass of  $M_{500} \sim 1.1 \times 10^{15} M_\odot$  (Abell et al. 1989; Struble & Rood 1999; Morandi et al. 2007; Planck Collaboration XVII 2016; Lotz et al. 2017). The bolometric X-ray luminosity is  $1.1 \times 10^{45} \text{ erg s}^{-1}$  (Morandi et al. 2007). A370 is the first cluster that was found to gravitationally lens a background galaxy (Hoag 1981; Lynds & Petrosian 1986; Soucail et al. 1987; Paczynski 1987). Since then, numerous works studied its properties (Kneib et al. 1993; Smail et al. 1996; Broadhurst et al. 2008; Richard et al. 2010; Umetsu et al. 2011; Lagattuta et al. 2017; Strait et al. 2018). The matter distribution of the cluster shows two main substructures, one centered on the northern and one on the southern brightest cluster galaxy (BCG), indicating a recent merging event (Richard et al. 2010). The velocity dispersion of each subcluster is about  $850 \text{ km s}^{-1}$  (Kneib et al. 1993). The dynamical unrelaxed state of the cluster is also suggested by the presence of X-ray surface brightness edges in the ICM, that may be related to shocks and/or cold fronts (Botteon et al. 2018).

Previous studies of A370 did not report on any extended radio emission in the cluster. Lah et al. (2009) analyzed the hydrogen gas content of 324 galaxies around the cluster based on GMRT observations. Wold et al. (2012) cataloged the radio sources in the cluster field, with VLA observation in A and B configurations. Some radio galaxies in the cluster field have also been studied (Smail et al. 2000; Hart et al. 2009).

## 2. Observations and data reduction

### 2.1. VLA observations

AS1063 and A370 were observed by the VLA in *L*- and *S*-bands with multiple array configurations (project: 16B-251, PI: R.J. van Weeren). The details of radio observations can be found in Table 2. Due to the low declination of AS1063, no D-array observations were obtained. The total on-source time for AS1063 and A370 are 13 h and 9 h, respectively. Recorded bandwidths are 1 GHz (*L*-band) and 2 GHz (*S*-band), covered by 16 spectral windows, with 64 channels each. The primary calibrators we used are 3C138 and 3C147. For the phase calibrator, we used J2214–3835 and J0149+0555 for AS1063 and A370, respectively.

The data were calibrated and reduced using the Common Astronomy Software Applications (CASA; McMullin et al. 2007) package, version 5.1.1. The data observed in different runs were processed separately using the same procedures. Each data set was first Hanning smoothed and data affected by antenna shadowing were flagged. Radio frequency interference (RFI) was automatically flagged using the CASA “tfcrop” mode in the flagdata task. Manual flagging was also applied if the antenna was not working properly by inspecting the bandpass, gain, and polarization solutions. The elevation dependent gain tables and antenna offsets positions were also applied. After that, the initial gain solutions of primary calibrators 3C147 and 3C138 were determined based on the central ten channels of a spectral window to remove the phase variation during calibrator observations. These initial gain solutions were applied to find the antenna-based delays and bandpass calibration tables. Applying the delay and bandpass solutions, we re-determined the gain

**Table 1.** Clusters properties.

Name	RA (J2000)	Dec (J2000)	Redshift	$M_{\text{SZ}}^{(a)}$ ( $10^{14} M_{\odot}$ )	$Y_{500}^{(b)}$ ( $10^{-4} \text{Mpc}^2$ )
Abell S1063	22 48 43.5	-44 31 44.0	0.346	$11.4 \pm 0.3$	$2.32 \pm 0.23$
Abell 370	02 39 50.5	-01 35 08.2	0.375	$7.6 \pm 0.6$	$1.75 \pm 0.46$

**Notes.** <sup>(a)</sup>From *Planck* measurements ([Planck Collaboration XXVII 2016](#)); <sup>(b)</sup>the  $Y_{5R_{500}}$  from *Planck* measurements ([Planck Collaboration XXVII 2016](#)) was rescaled to  $Y_{500} = Y_{5R_{500}}/1.79$  ([Arnaud et al. 2010](#)).

**Table 2.** Log of radio observations.

Name	Observation	Observing date	Frequency coverage (GHz)	Channel width (MHz)	Integration time (s)	On-source time (hr)
Abell S1063	GMRT 325 MHz	25 Feb 2017	0.31–0.34	0.13	16	4.8
		26 Aug 2017	0.31–0.34	0.13	4	4.1
	<i>L</i> -band C-array	24 Jun 2017	1–2	1	5	2.0
		25 Jun 2017	1–2	1	5	2.0
	<i>L</i> -band B-array	13 Oct 2017	1–2	1	3	1.3
		07 Nov 2017	1–2	1	3	1.3
	<i>S</i> -band C-array	17 Jun 2017	2–4	2	5	1.9
		18 Jun 2017	2–4	2	5	1.9
	<i>S</i> -band B-array	02 Oct 2017	2–4	2	3	1.2
		04 Oct 2017	2–4	2	3	1.2
Abell 370	GMRT 325 MHz	07 Jan 2017	0.31–0.34	0.13	8	4.8
		05 Mar 2017	0.31–0.34	0.13	4	5.7
		01 Aug 2017	0.31–0.34	0.13	4	4.7
	<i>L</i> -band D array	11 Feb 2017	1–2	1	5	1.5
	<i>L</i> -band C array	20 May 2017	1–2	1	5	3.2
	<i>S</i> -band D array	11 Feb 2017	2–4	2	5	1.3
	<i>S</i> -band C array	28 May 2017	2–4	2	5	3.1

solutions for our primary calibrators using the full bandwidth, apart from a few noisy edge channels. Next, we determined the gain solutions for phase calibrators. The flux scale of primary calibrators was calculated from the [Perley & Butler \(2013\)](#) model and applied to the phase calibrators. As a final step, we applied all the solutions to the target field and averaged the data by a factor of 3 and 4 in time and frequency, respectively. To remove additional RFI, we performed a last flagging step with **AOFagger** ([Offringa et al. 2010](#)) on the target field data.

To refine the calibration of the target field, two rounds of phase-only self-calibration were applied. This was followed by a few amplitude and phase self-calibration rounds until the image quality did not improve further. Additional bad data were flagged during the self-calibration by visually inspecting the gain solutions. The imaging during the self-calibration was done with **CASA**, using the full bandwidth to make a deep Stokes I image with Briggs weighting (robust = 0; [Briggs 1995](#)). To account for the non-coplanarity of the array, w-projection with 256 planes ([Cornwell 2008](#)) was employed. The clean masks were created by the Python Blob Detector and Source Finder (**PyBDSF**; [Mohan & Rafferty 2015](#)) package. For the wide-band deconvolution, the spectral index was taken into account with “nterms” of 3 ([Rau & Cornwell 2011](#)). After the self-calibration, we combined the data sets from the different array configurations

in the same frequency band and run an extra self-calibration step to align them. The primary beam attenuation was also corrected for.

## 2.2. GMRT observations

AS1063 and A370 were observed with GMRT at 325 MHz with a bandwidth of 33.3 MHz (project code: 31\_037, PI: R.J. van Weeren) on different observing sessions (see Table 2). We used the Source Peeling and Atmospheric Modeling (SPAM; [Intema et al. 2009](#)) pipeline to process the continuum observations obtained with the GMRT software correlator backend (GSB). The details of SPAM pipeline can be found in [Intema \(2014\)](#), [Intema et al. \(2017\)](#). We combined the multiple data sets for the single targets during the SPAM processing. To summarize, the SPAM pipeline performs direction-independent and direction-dependent calibration. The main steps include the averaging and flagging of data, bandpass and flux scale calibration ([Scaife & Heald 2012](#)), initial phase-only calibration, and direction dependent calibration and ionospheric modeling using the bright sources in the primary beam.

The output from SPAM was imaged using **CASA** with w-projection (256 planes) and Briggs weighting, robust 0. The details of imaging parameters can be found in Table 3. For the GMRT data, “nterms” of 2 was adopted.

### 2.3. Flux density uncertainties and compact source subtraction

Throughout the paper, the uncertainties on the flux density measurements are estimated using

$$\sigma = \sqrt{\sigma_{\text{cal}}^2 + \sigma_{\text{R}}^2}, \quad (1)$$

where the statistical error  $\sigma_{\text{R}} = \sigma_{\text{rms}} \times \sqrt{N_{\text{beams}}}$ , with the noise level of image  $\sigma_{\text{rms}}$  and the number of beams  $N_{\text{beams}}$  covered by the source. The absolute flux-scale calibration uncertainty is  $\sigma_{\text{cal}} = fS_{\text{int}}$ , with  $S_{\text{int}}$  the flux density and  $f$  the fractional uncertainty of the flux-scale. We adopt  $f = 0.1$  for the GMRT and  $f = 0.05$  for the VLA.

To search for and characterize the diffuse emission in the two clusters, the contribution from compact sources needs to be removed. We did this by first imaging the combined data sets of each frequency band using  $\text{robust} = -1$  weighting and an inner uv-cut of  $3\text{k}\lambda$ . At the redshift of our clusters,  $3\text{k}\lambda$  corresponds to about 400 kpc. We then computed the visibility data of this model for the entire uv-data range and subtracted these from the calibrated visibility data using the CASA task `uvsub`.

For imaging possible diffuse emission in the clusters, we used multiscale clean (Cornwell 2008) with scales of [0, 3, 7, 25, 75]<sup>2</sup>, uvtapers, and Briggs weighting. The details of the imaging parameters can be found in Table 3. The integrated flux densities for diffuse emission, or upper limits, were computed from these images. Based on the residuals, at the location of bright compact sources outside the cluster region, we estimate the error on the compact subtraction is less than 1%. To provide an alternative estimate for the integrated flux densities, we also measured the integrated flux densities using images that still contained the compact sources. The contribution of the compact sources was then removed by manually computing their integrated flux densities on our images with the highest spatial resolution (Table 3). In this case, we include the uncertainty on the subtraction of the compact sources, on the total uncertainty of the flux density of the diffuse emission, using standard error propagation. In all cases, the results using our two methods gave results that were consistent. For completeness, we report the flux densities using the latter method in Table 4 with footnotes.

### 2.4. Spectral index maps

To map the spectral index distribution, we used an inner uv-cut of  $0.15\text{k}\lambda$  for AS1063 and  $0.22\text{k}\lambda$  for A370, to sample the same spatial scales at all three frequency bands. We note that for A370, due to the non-detection of diffuse emission in the  $S$ -band, we chose the shortest baseline only from on  $L$ -band and 325 MHz data to maximally recover the diffuse flux. The CASA tasks `imsmooth` and `imregrid` were used to align the beam shapes and pixel grids. Only pixel values larger than  $3\sigma_{\text{rms}}$  were used to calculate the spectral index maps. The integrated flux densities were also measured from the same images that were used to construct spectral index maps.

### 2.5. X-ray observations

Abell S1063 was observed with the *Chandra* X-ray Observatory (ACIS-I detectors, VF mode, ObsIds 4966 – PI Romer, 18611, 18818 – PI Kraft). Abell 370 was observed with ACIS-I and S detectors, ObsIds 515 and 7715 – PI Garmire. The data were

**Table 3.** Imaging information.

AS1063	uv-cut ( $\text{k}\lambda$ )	uvtaper (")	beam ("×")	$\sigma_{\text{rms}}$ ( $\mu\text{Jy beam}^{-1}$ )
325 MHz	–	–	$26.0 \times 9.0$	46
325 MHz	>0.15	15	$45.0 \times 16.0$	96
$L$ -band	–	–	$26.0 \times 9.0$	21
$L$ -band	>0.15	15	$45.0 \times 16.0$	40
$S$ -band	–	–	$26.0 \times 9.0$	11
$S$ -band	>0.15	15	$45.0 \times 16.0$	24
A370	uv-cut ( $\text{k}\lambda$ )	uvtapers (")	Beam ("×")	$\sigma_{\text{rms}}$ ( $\mu\text{Jy beam}^{-1}$ )
325 MHz	–	–	$11.9 \times 8.6$	62
325 MHz	>0.22	20	$25.0 \times 22.0$	161
$L$ -band	–	–	$14.8 \times 11.5$	26
$L$ -band	>0.22	20	$25.0 \times 22.0$	34
$S$ -band	–	–	$8.5 \times 7.3$	9
$S$ -band	–	20	$25.0 \times 22.0$	18

**Notes.** All images are made with Briggs weighting, robust 0.

reduced using the software CHAV which follows the processing described in Vikhlinin et al. (2005), applying the calibration files CALDB 4.7.1. The data processing includes corrections for the time dependence of the charge transfer inefficiency and gain, and a check for periods of high background. Also, readout artifacts were subtracted and standard blank sky background files were used for background subtraction. We show the combined images of all observations in the 0.5–2.0 keV energy band in Sect. 3.

*XMM-Newton* observations were processed with the XMM-SAS v16.0.0 software<sup>3</sup>. The calibrated event files were generated from raw data by running the tasks `emchain` and `epchain`. Throughout this analysis, we only considered single pixel events for the pn data (i.e., `PATTERN == 0`) and single, double, triple, and quadruple events (i.e.,  $\text{PATTERN} \leq 12$ ) for MOS. In addition, we removed all the events next to CCD edges and next to bad pixels (i.e., `FLAG == 0`) and we applied the pn out-of-time correction. All the data sets were cleaned for periods of high background due to solar flares following the two stage filtering process extensively described in Lovisari et al. (2011). The task `edetect-chain` has been used to detect the point-like sources which were then excluded from the event files. The background event files were cleaned by applying the same `PATTERN` selection, flare rejection criteria and point-source removal used for the observation events.

The background-subtracted and exposure-corrected image for A370 (see Fig. 8) has been obtained with MOS data only in the 0.3–7 keV band using a binning of 40 physical pixels corresponding to a resolution of 2 arcsec, and smoothed with a Gaussian of FWHM of 6 arcsec. The background subtraction was performed using a combination of blank-sky-field and filter-wheel-closed observations as described in Lovisari et al. (2017).

The temperature profile of AS1063 has been derived using successive annular regions centered on the X-ray peak. The size of the annuli was determined by requiring that the width is larger than 0.5', to minimize the flux redistribution due to the PSF, and a  $S/N > 100$  to measure the temperatures with an accuracy of  $\sim 10\%$  (68% confidence limit). The spectral fitting procedure and the modeling of the different background components is fully described in Lovisari & Reiprich (2019).

<sup>2</sup> The scales are in unit of pixels. The beam is sampled by ~4 pixels.

<sup>3</sup> <https://www.cosmos.esa.int/web/xmm-newton/sas>

**Table 4.** Properties of the radio sources for Abell S1063 and Abell 370, labeled in Figs. 1 and 8.

Name	RA (J2000)	Dec (J2000)	$S_{325\text{ MHz}}$ (mJy)	$S_{1.5\text{ GHz}}$ (mJy)	$S_{3\text{ GHz}}$ (mJy)	$\alpha_{325}^{1500}$	$\alpha_{1500}^{3000}$
AS1063 Halo <sup>(a)</sup>	22 48 43.5	-44 31 44.0	$24.3 \pm 2.5$	$5.8 \pm 0.4$	$1.7 \pm 0.2$	$-0.94 \pm 0.08$	$-1.77 \pm 0.20$
AS1063 Source A	22 48 44.0	-44 31 51.85	$8.5 \pm 1.1$	$2.1 \pm 0.2$	$1.0 \pm 0.1$	$-0.93 \pm 0.10$	$-1.03 \pm 0.15$
AS1063 Source B	22 48 41.8	-44 31 56.48	$2.2 \pm 0.3$	$0.7 \pm 0.1$	$0.3 \pm 0.1$	$-0.80 \pm 0.12$	$-1.07 \pm 0.23$
AS1063 Source C	22 48 44.6	-44 30 09.59	$40.7 \pm 4.2$	$10.0 \pm 0.5$	$4.5 \pm 0.2$	$-0.92 \pm 0.08$	$-1.16 \pm 0.10$
AS1063 Source D	22 48 49.3	-44 30 44.58	$37.8 \pm 3.8$	$5.6 \pm 0.3$	$1.8 \pm 0.1$	$-1.24 \pm 0.07$	$-1.61 \pm 0.11$
A370 Halo <sup>(a)</sup>	02 39 52.0	-01 35 12.0	$20.0 \pm 2.3$	$3.7 \pm 0.3$	<1.3	$-1.10 \pm 0.09$	<-1.51
A370 Source A	02 39 52.7	-01 34 19.8	$0.9 \pm 0.1$	$0.2 \pm 0.1$	-	$-1.06 \pm 0.18$	-
A370 Source B	02 39 53.1	-01 34 56.0	-	$0.11 \pm 0.01$ <sup>(b)</sup>	-	-	-
A370 Source C	02 39 50.9	-01 35 42.4	$3.1 \pm 0.3$	$1.5 \pm 0.1$	$0.8 \pm 0.1$	$-0.48 \pm 0.09$	$-0.91 \pm 0.16$
A370 Source D	02 39 52.1	-01 35 56.8	$1.2 \pm 0.6$	$0.3 \pm 0.1$	$0.2 \pm 0.1$	$-0.86 \pm 0.34$	$-0.91 \pm 0.75$
A370 Source E	02 39 55.4	-01 34 07.9	$15.5 \pm 2.0$	$7.1 \pm 0.7$	$4.4 \pm 0.4$	$-0.51 \pm 0.10$	$-0.70 \pm 0.19$
A370 Source F	02 39 56.5	-01 34 29.0	$4.5 \pm 1.0$	$2.0 \pm 0.4$	$1.3 \pm 0.1$	$-0.53 \pm 0.19$	$-0.64 \pm 0.28$

**Notes.** <sup>(a)</sup> Alternative flux densities by manually subtraction the contribution of compact sources. For AS1063:  $S_{325\text{ MHz}} = 25.3 \pm 2.7$  mJy,  $S_{1.5\text{ GHz}} = 5.1 \pm 0.5$  mJy,  $S_{3\text{ GHz}} = 1.4 \pm 0.2$  mJy; for A370:  $S_{325\text{ MHz}} = 23.9 \pm 2.9$  mJy,  $S_{1.5\text{ GHz}} = 2.7 \pm 0.8$  mJy,  $S_{3\text{ GHz}} < 1.7$  mJy. <sup>(b)</sup>The southern BCG is blended with other sources. Here we adopt the 1.4 GHz flux density from Wold et al. (2012).

### 3. Results

#### 3.1. Abell S1063

A *Spitzer* infrared (IR) image of AS1063, overlaid with our 1.5 GHz radio contours is presented in Fig. 1. Four compact radio sources are detected in the cluster vicinity, labeled A to D in Fig. 1. In the central regions of the cluster more extended diffuse emission is also detected. The properties of the radio sources are listed in Table 4.

Source A, namely rxj2248\_17936<sup>4</sup> or 2MASX J22484405-4431507, is the BCG in AS1063. The integrated flux densities of the BCG are  $8.5 \pm 1.1$  mJy at 325 MHz,  $2.1 \pm 0.2$  mJy at 1.5 GHz, and  $1.0 \pm 0.1$  mJy at 3.0 GHz. This corresponds to a spectral index of about -1, typical for a cluster AGN. Source B (rxj2246\_18112) is a background galaxy at redshift of 0.61, identified as [GVR2012] 878 by Gómez et al. (2012). Source C (rxj2248\_19890) is the brightest radio galaxy in the cluster field, located north of the cluster center.

Source D (rxj2248\_18479) is a radio galaxy with a radio tail at the northeast of the cluster. The radio tail is connected to the diffuse emission and the tail length is  $\sim 140$  kpc at 1.5 GHz (see, Fig. 1). The tail length increase at 325 MHz to  $\sim 340$  kpc. The integrated flux densities are  $37.8 \pm 3.8$  mJy at 325 MHz,  $5.6 \pm 0.3$  mJy at 1.5 GHz, and  $1.8 \pm 0.1$  mJy at 3.0 GHz. The corresponding spectral indices are  $\alpha_{325}^{1500} = -1.24 \pm 0.07$  and  $\alpha_{1500}^{3000} = -1.61 \pm 0.11$ . Such spectral behavior indicates a high frequency break, the result of the radiative losses of the synchrotron emitting electrons.

In Fig. 2 we show the *Chandra* 0.5–2.0 keV X-ray image of the cluster. Radio contours at 0.325, 1.5 and 3.0 GHz are overlaid in the various panels. The emission from compact sources was subtracted from the uv-data in these radio images (see Sect. 2.3), to better determine the properties of the diffuse radio emission. Central diffuse emission is detected at all three frequencies which roughly follows the distribution of the thermal ICM. We further investigate the connection between the thermal and nonthermal emission by comparing the X-ray and radio surface brightness evaluated in the same regions of the *Chandra* 0.5–2.0 keV and GMRT 325 MHz source subtracted

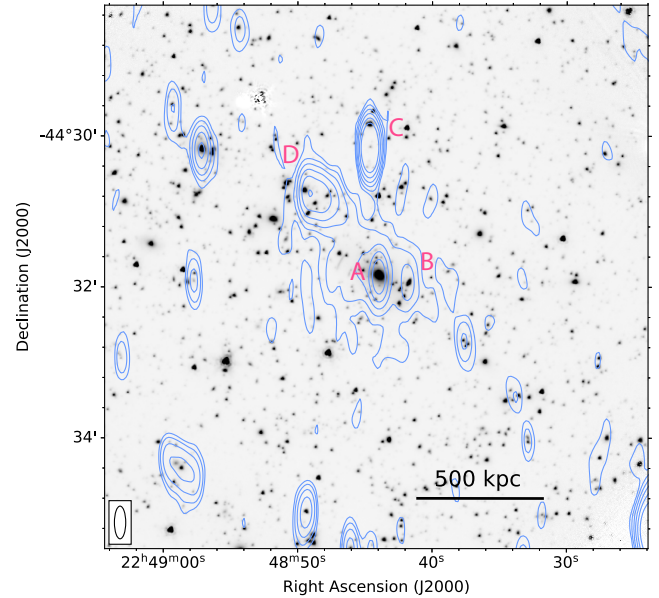


**Fig. 1.** *Spitzer* 3.6  $\mu\text{m}$  IRAC image of AS1063 overlaid with VLA 1.5 GHz radio contours. Contour levels are drawn at [1, 2, 4, 8, 16, 32]  $\times 3\sigma_{\text{rms}}$ , where  $\sigma_{\text{rms}} = 21 \mu\text{Jy beam}^{-1}$ . Due to the low declination of the cluster, the radio beam is quite elongated ( $26'' \times 9''$ ). Compact radio sources are labeled A to D, see also Fig. 7.

images. Regions were chosen based on the  $3\sigma$  level emission of the GMRT image, where 19 beam independent regions were identified. The plot of the radio versus X-ray surface brightness is reported in Fig. 3, where regions with higher X-ray surface brightness seems associated to regions with higher radio surface brightness. This trend has been observed for a number of radio halos (Govoni et al. 2001; Rajpurohit et al. 2018; Hoang et al. 2019; Cova et al. 2019). Despite the small number of data points, we fit the data with a power-law in the form  $I_{\text{radio}} \propto I_{\text{X-ray}}^b$  and obtain a slope  $b = 0.55 \pm 0.04$  which is within the range of values found in the literature. From the 1.5 GHz image, a slope of  $0.48 \pm 0.07$  is obtained, which is consistent with the value from the 325 MHz image. The largest physical extent of the diffuse emission is  $\sim 700$  kpc at 1.5 GHz and this increases

<sup>4</sup> The ID number in CLASH *Spitzer* catalog (Postman et al. 2012).

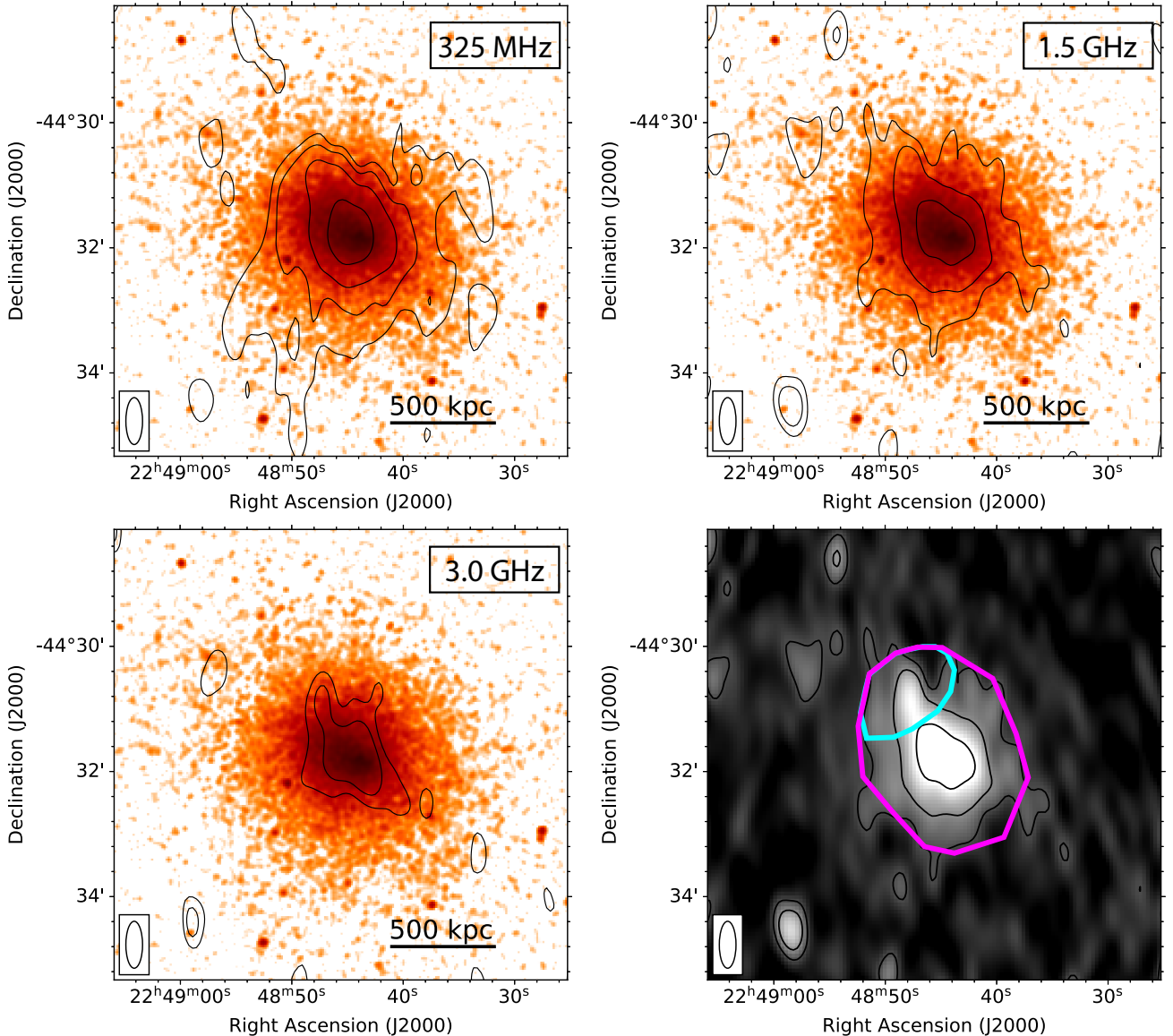


**Fig. 2.** *Chandra* image of AS1063 overlaid with the radio contours of diffuse emission in AS1063 at three frequencies (325 MHz, top left; 1.5 GHz, top right; 3.0 GHz, bottom left). *Chandra* images are all in the energy band 0.5–2.0 keV with pixel size  $4 \times 0.492''$  and smoothed with a Gaussian with scale of 3 pixels across. Contour levels are drawn at  $[1, 2, 4, 8, \dots] \times 3\sigma_{\text{rms}}$ , where  $\sigma_{325 \text{ MHz}} = 96 \mu\text{Jy beam}^{-1}$ ,  $\sigma_{1.5 \text{ GHz}} = 40 \mu\text{Jy beam}^{-1}$ ,  $\sigma_{3.0 \text{ GHz}} = 24 \mu\text{Jy beam}^{-1}$ . Compact radio sources were subtracted in all radio images. The inner uv-cut of  $0.15 \text{ k}\lambda$  is adopted for all radio images. Bottom right: VLA *L*-band image of AS1063 depicting the region where we extract the integrated flux densities. The cyan polygon indicates the region where the diffuse AGN component is subtracted from the total flux measurement (magenta polygon).

to  $\sim 1.2$  Mpc at 325 MHz. Besides the central diffuse emission, we also detect remnant emission from the tail of source D (also see, Fig. 1). Because of the extended nature of the tail, it is not possible to fully remove this in the source subtraction processes. To determine the integrated flux density of the central diffuse emission we therefore exclude the area indicated by the cyan polygon in Fig. 2 (bottom right panel). We used the same extraction region for the integrated flux density for all three frequencies (see Fig. 2). The uncertainties are computed as described in Sect. 2.3.

The flux densities of the central diffuse emission are  $24.3 \pm 2.5 \text{ mJy}$ ,  $5.8 \pm 0.4 \text{ mJy}$ , and  $1.7 \pm 0.2 \text{ mJy}$ , at 325 MHz, *L*-band, and *S*-band, respectively. Using the observed flux densities, we find that the spectral index steepens at high frequencies with  $\alpha_{325}^{1500} = -0.94 \pm 0.08$ , and  $\alpha_{1500}^{3000} = -1.77 \pm 0.20$ . If we adjust the size of the extraction region to the extension of the radio

halo at 325 MHz, the derived spectral indices remain consistent with each other within the uncertainties. In Fig. 4, we present the integrated spectrum of the diffuse emission. A single power-law fit is unacceptable with  $\chi^2/\text{d.o.f.} = 17.7$ , showing the spectrum deviates from a power-law shape.

We conclude that the diffuse emission we find in AS1063 is a new radio halo based on the lack of a clear optical counterpart, the central location, and the large physical extent. From the flux density measurement in the *L*-band, we calculate a monochromatic radio halo power of  $P_{1.4 \text{ GHz}} = (2.63 \pm 0.18) \times 10^{24} \text{ W Hz}^{-1}$  using the equation

$$P_{1.4 \text{ GHz}} = 4\pi D_L^2 S_{1.4 \text{ GHz}} (1+z)^{-(\alpha+1)}, \quad (2)$$

where  $D_L$  is the luminosity distance. Here, we adopted  $\alpha = -1.14$ , and derived the flux density at 1.4 GHz  $S_{1.4 \text{ GHz}}$  from  $S_{1.5 \text{ GHz}}$  (scaling with the mentioned spectral index).

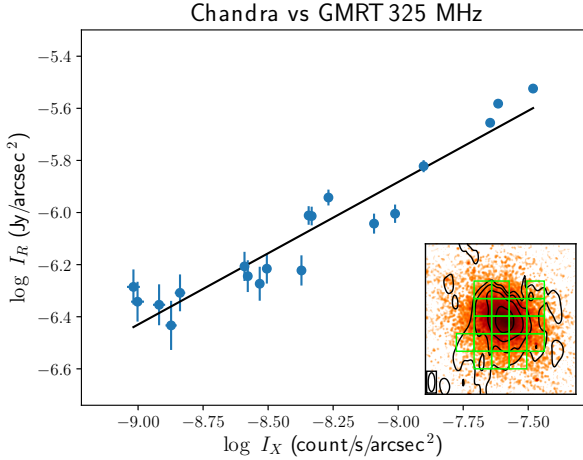


**Fig. 3.** X-ray versus radio surface brightness (SB) for AS1063. The red line shows the best fit power-law  $I_{\text{radio}} \propto I_{\text{X-ray}}^{0.55 \pm 0.04}$ . The inset shows the region (green grid) where we measured the corresponding surface brightness.

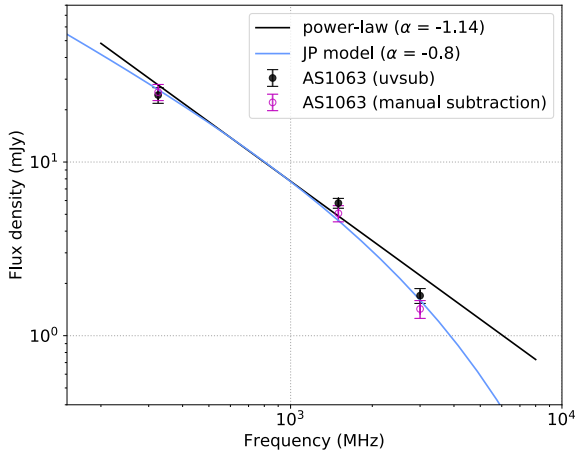


**Fig. 4.** Integrated flux densities for the halo in AS1063 at 325 MHz, 1.5 GHz, and 3.0 GHz, measured by two methods. The black line shows a single power-law fit with spectral index  $\alpha = -1.14$ . The JP model has an injection spectral index of  $-0.8$ .

Statistical studies of radio halos have revealed a correlation between radio halo power and cluster mass (e.g., Cassano et al. 2006, 2013; Basu 2012; Sommer & Basu 2014; Martinez Aviles et al. 2016). The general idea is that a small fraction of the gravitational energy is converted into relativistic electrons during a cluster merger. The amount of energy released correlates with the cluster mass and results in the relation between radio power and cluster mass. Adopting the cluster sample from Cassano et al. (2013), we over-plot our radio measurement of the halo emission on the  $P_{1.4\text{GHz}} - Y_{500}$  diagram in Fig. 5.  $Y_{500}$  is the integrated SZ signal, estimated from  $Y_{5R_{500}}$  as  $Y_{500} = Y_{5R_{500}}/1.79$  (Arnaud et al. 2010). The  $Y_{5R_{500}}$  is obtained from Planck Collaboration XXVII (2016). Unlike the X-ray luminosity,  $Y_{500}$  is a more robust mass tracer as it less affected by the cluster's dynamical state (Motl et al. 2005; Nagai 2006). Figure 5 shows that the radio power of AS1063 is slightly lower than most clusters in this  $Y_{500}$  range, but consistent within the expected scatter.

We constructed spectral index maps between 0.325 and 1.5 GHz, and between 1.5 and 3.0 GHz to characterize the spectral index distribution across the halo of AS1063 with resolution

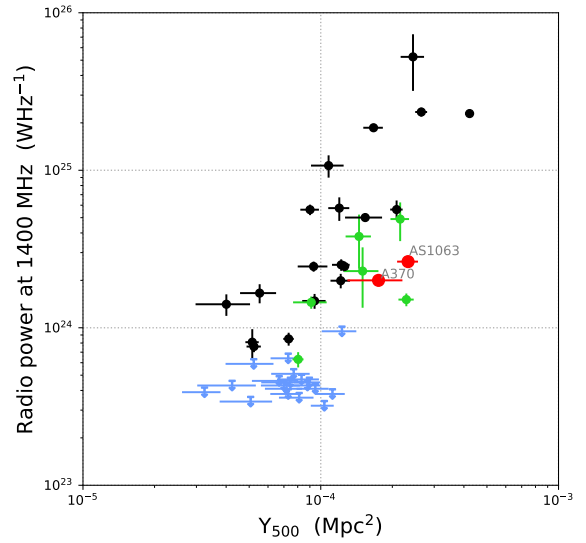


**Fig. 5.** Distribution of radio halos in the  $P_{1.4\text{GHz}} - Y_{500}$  diagram. Different symbols are used to represent the radio halos (black dots), radio halos with ultra-steep spectra (green dots) and the upper limits (blue arrows) from Cassano et al. (2013). AS1063 and A370 are shown as red dots.

of  $45'' \times 16''$ , see Fig. 6. The imaging details can be found in Sect. 2.4. Spectral index uncertainty maps can be found in Appendix A.

The spectral index between 0.325 and 1.5 GHz ranges from  $\sim -0.8$  at the eastern part of the halo to  $\sim -1.1$  at the western part. The halo has steeper values between 1.5 GHz and 3.0 GHz, varying from  $\sim -1.7$  at the eastern side to  $\sim -1.25$  at the western side. However, these east-west trends are not very significant, considering the spectral index uncertainty of  $\sim 0.15$  and  $\sim 0.25$  in  $\alpha_{325}^{1500}$  and  $\alpha_{325}^{3000}$  maps, respectively.

Figure 7 shows the spectral index map of source D between 325 MHz and 1.5 GHz. The corresponding uncertainty map can be found in Fig. A.2. Source D shows a clear spectral index gradient along the radio tail. The spectral index steepens from  $\sim -0.6$  at location of the IR counterpart to  $\sim -2.4$  at the tail end. Such a trend is expected as the result of the radiative losses of electrons.

### 3.2. Abell 370

A *Spitzer* image of A370 with 325 MHz radio contours overlaid is presented in Fig. 8. A number of compact radio sources are detected in the cluster field. Wold et al. (2012) analyzed 1.4 GHz VLA observations of the A370 cluster field in the A and B configurations. Their radio source catalog is over plotted on Fig. 8. We also label several radio sources in the cluster region, source A to F. The flux densities of these sources are reported in Table 4.

There are two BCGs in A370 and both show radio emission associated with an AGN. Source A, the northern BCG is detected at 325 MHz and 1.5 GHz. The flux densities are  $S_{325\text{MHz}} = 0.86 \pm 0.10$  mJy and  $S_{1.5\text{GHz}} = 0.17 \pm 0.04$  mJy, corresponding to a spectral index of  $-1.06 \pm 0.18$ . The southern BCG marked as B, blends with other nearby radio sources in our relatively low resolution image with a beam size of  $11.9'' \times 8.6''$ . The high resolution 1.4 GHz image of Wold et al. (2012) shows a separate radio source associated with the BCG with a flux density of 0.11 mJy.

Some very faint extended emission is found in the southern part of the cluster near source B and south of it (see Fig. 8).

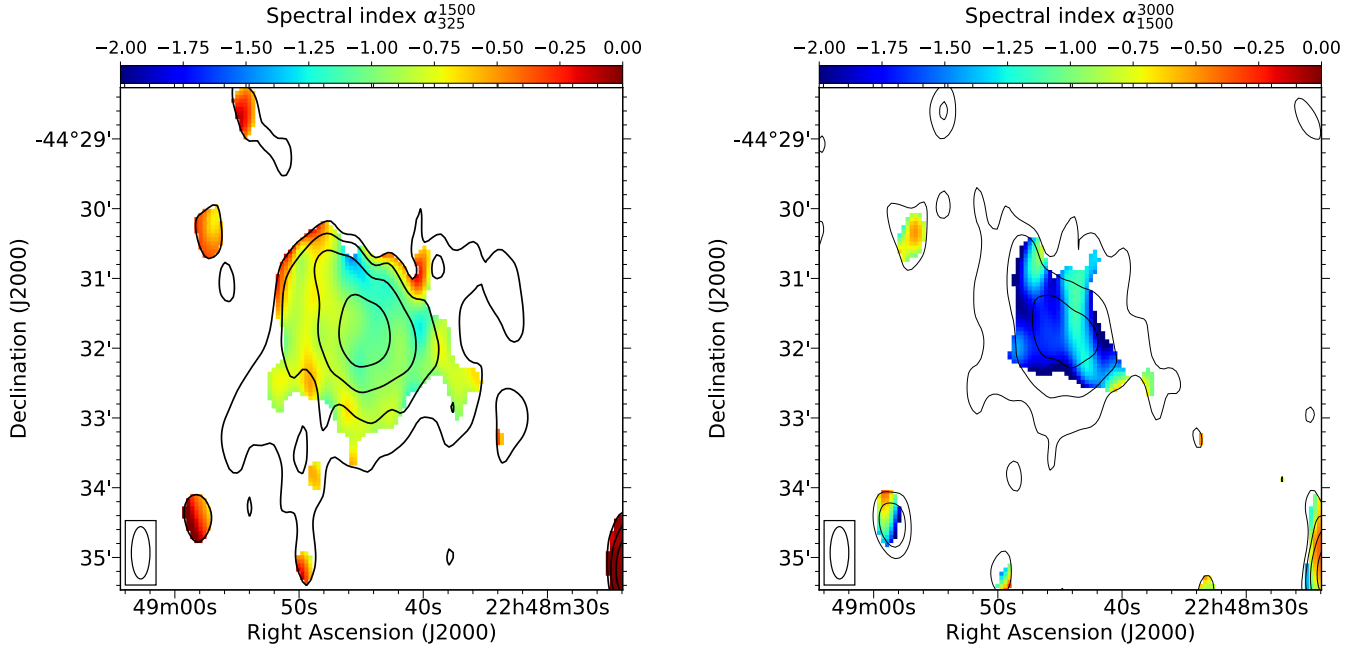


**Fig. 6.** Spectral index maps of AS1063 between 325 MHz and 1.5 GHz (*left*), and between 1.5 GHz and 3.0 GHz (*right*). The radio contours are from the 325 MHz (*left*) and 1.5 GHz (*right*) images. These maps were created from the compact source subtracted uv-data. The beam size is indicated in the bottom left corner. Contour levels are drawn at  $[1, 2, 4, 8, \dots] \times 3\sigma_{\text{rms}}$ , where  $\sigma_{325 \text{ MHz}} = 96 \mu\text{Jy beam}^{-1}$ ,  $\sigma_{1.5 \text{ GHz}} = 40 \mu\text{Jy beam}^{-1}$ .

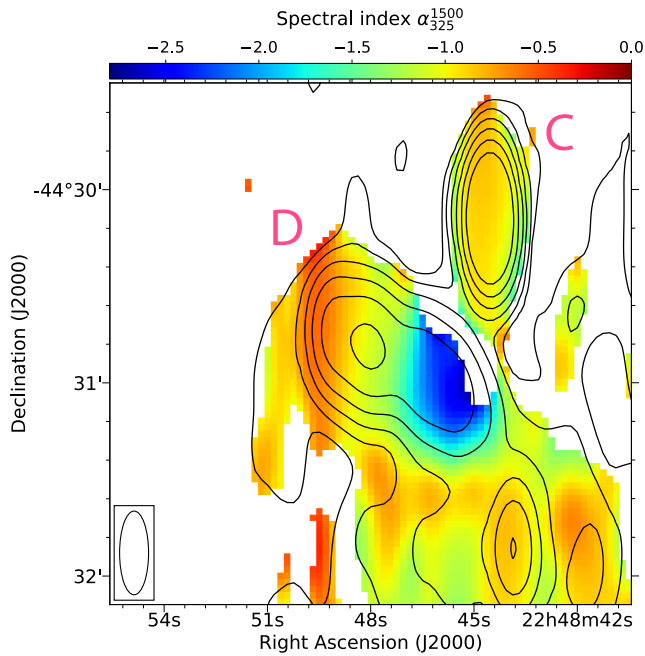


**Fig. 7.** Spectral index map of source D in AS1063 between 325 MHz and 1.5 GHz. The radio contours are from the GMRT 325 MHz image. The beam size is  $26.0'' \times 9.0''$  and indicated in the bottom left corner. Contour levels are drawn at  $[1, 2, 4, 8, 16, 32, \dots] \times 5\sigma_{\text{rms}}$ , where  $\sigma_{\text{rms}} = 46 \mu\text{Jy beam}^{-1}$ .

To better bring out the diffuse emission we made low-resolution compact source subtracted images (for details see Sect. 2.3). A *XMM-Newton* X-ray image, with radio contours at 0.325 and 1.5 GHz overlaid, is displayed in Fig. 9. For completeness, a *Chandra* image is also shown, overlaid with radio contours at 3 GHz. Diffuse emission is detected at 325 MHz and 1.5 GHz. The total extent of the diffuse emission is about 500–700 kpc. The surface brightness of this emission peaks at the location

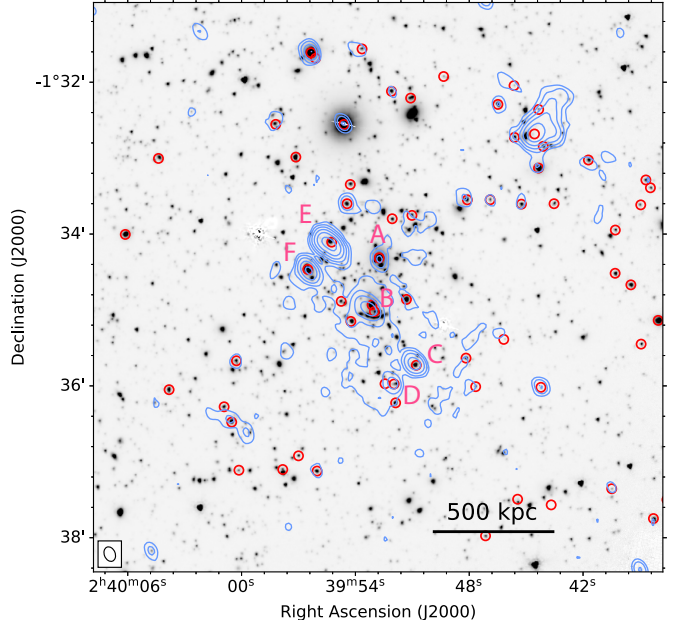


**Fig. 8.** *Spitzer* 3.6  $\mu\text{m}$  IRAC image of A370 overlaid with the GMRT 325 MHz radio contours. The beam size is  $11.9'' \times 8.6''$ . Contour levels are drawn at  $[1, 2, 4, 8, 16, 32] \times 3\sigma_{\text{rms}}$ , where  $\sigma_{\text{rms}} = 62 \mu\text{Jy beam}^{-1}$ . Compact radio sources are indicated with red labels from A to F. The red circles mark the 1.4 GHz radio source catalog from Wold et al. (2012).

of the southern BCG. We note that the emission at north-west periphery of the cluster are residuals from an extended tailed radio galaxy that is not completely subtracted from uv-data. The flux density of the radio halo is  $20.0 \pm 2.3 \text{ mJy}$  at 325 MHz and  $3.7 \pm 0.3 \text{ mJy}$  at 1.5 GHz. For the non-detection at 3.0 GHz we determine a  $3\sigma$  upper limit of  $< 1.3 \text{ mJy}$ . The region where we measured the flux densities is indicated in Fig. 9. The corresponding spectral indices are  $\alpha_{325}^{1500} = -1.10 \pm 0.09$ , and  $\alpha_{1500}^{3000} < -1.51$ .

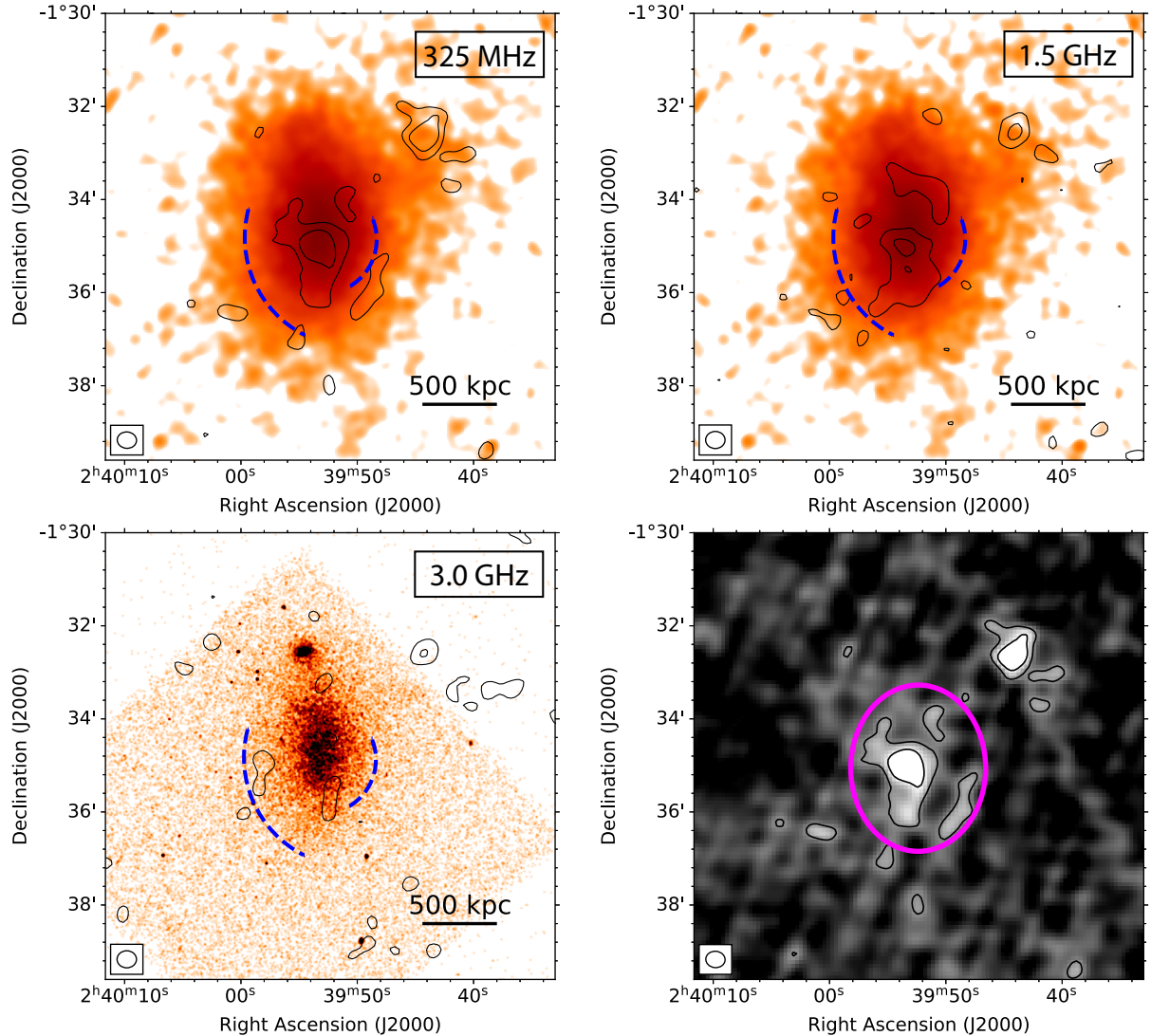


**Fig. 9.** *XMM-Newton* 0.3–7 keV image of A370 overlaid with the radio contours with compact sources subtracted from the uv-data (325 MHz, top left; 1.5 GHz, top right). All the point source in *XMM-Newton* image are removed and smoothed with a Gaussian with scale of 3 pixels across. The Blue dashed curves show the surface brightness edges found by Botteon et al. (2018). Bottom left: *Chandra* 0.5–2.0 keV image overlaid with the 3.0 GHz radio contours with compact sources subtracted from the uv-data. The radio beam size is  $25.0'' \times 22.0''$ . Contour levels are drawn at  $[1, 2, 4, 8, \dots] \times 3\sigma_{\text{rms}}$ , where  $\sigma_{325\text{MHz}} = 161 \mu\text{Jy beam}^{-1}$ ,  $\sigma_{1.5\text{GHz}} = 34 \mu\text{Jy beam}^{-1}$ ,  $\sigma_{3.0\text{GHz}} = 18 \mu\text{Jy beam}^{-1}$ . The inner uv-cut of  $0.22 k\lambda$  is adopted for 325 MHz and 1.5 GHz images. Bottom right: GMRT 325 MHz image of A370 depicting the region (magenta ellipse) where we extract the integrated flux densities.

We classify the extended emission in A370 as a radio halo based on the lack of a clear optical counterpart, physical extent, and location in the cluster. Deeper observations are needed to determine the full extent of the radio halo given its low surface brightness. We compute a monochromatic radio power at 1.4 GHz of  $P_{1.4\text{GHz}} = (2.00 \pm 0.16) \times 10^{24} \text{ W Hz}^{-1}$ , where we take  $\alpha = -1.1$ . The radio halo power is consistent with that expected from the known scaling relations (Cassano et al. 2013), see Fig. 5. We do not compute spectral index maps of the radio halo as the emission is barely detected at three times the map noise level.

Botteon et al. (2018) detected two X-ray surface brightness edges on the west and east side of the cluster, which is shown as blue dashed curves in Fig. 9. Due to the limited number of X-ray counts, the nature (cold front or shock) of these edges could not be determined. No clear correspondence between the edges and radio emission halo emission is found.

## 4. Discussion

### 4.1. Merger scenarios and nature of the radio halos

The presence of a radio halo in the massive merging cluster A370 is expected based on the dynamical state of this cluster. A370 has a clear bimodal mass distribution, indicating a major merger event (Richard et al. 2010). This is also supported by the presence of X-ray surface brightness edges (Botteon et al. 2018). The radio halo in A370 thus supports the general scenario that radio halos trace particles that are re-accelerated by merger induced turbulence.

The dynamical state of AS1063 is key to interpreting the nature and formation scenario for its radio halo. However, the dynamical state of AS1063 is still under debate. The presence of a single BCG and a morphological analysis from *XMM-Newton* observations suggest a relaxed dynamical state (Lovisari et al. 2017). This X-ray analysis used the concentration

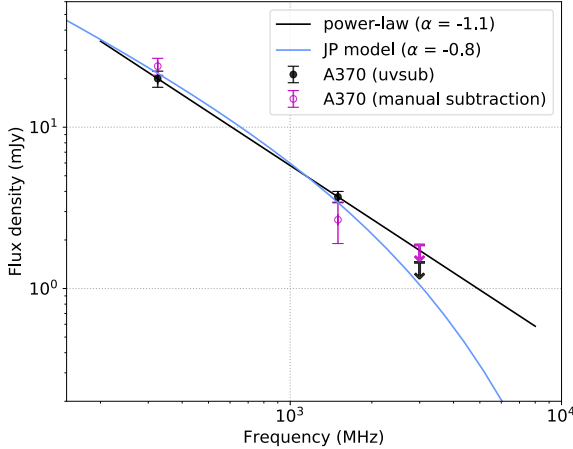


**Fig. 10.** Integrated flux densities and  $3\sigma$  upper-limits for the halo in A370 at 325 MHz, 1.5 GHz, and 3.0 GHz, measured by two methods. The black line shows a single power-law with spectral index  $\alpha = -1.1$ . The JP model has an injection spectral index of  $-0.8$ .

value, power ratio, and centroid shift. On the other hand the offset between the galaxy distribution and the peak of the X-ray emission, high global X-ray temperature, and weak lensing analysis indicate an ongoing major merger event (Gómez et al. 2012; Gruen et al. 2013).

Radio minihalos exclusively occur in cool core clusters. In addition, typically their sizes are a few hundreds of kpc and the emission from the minihalo is confined to the cooling region (e.g., Mazzotta & Giacintucci 2008; Giacintucci et al. 2017, 2019). To determine whether AS1063 hosts a cool core we derived a radial temperature profile from the *XMM-Newton* data, see Sect. 2.5 for more details. This radial profile is displayed in Figure 11. The central two bins of this profile ( $<250$  kpc) show temperatures about 10 keV which indicate AS1063 has a rather hot-core. This result is consistent with the conclusion of the presence of a hot-core based on *Chandra* data by Gómez et al. (2012). We thus conclude that the diffuse emission in AS1063 cannot be classified as a radio minihalo, also in line with the rather large extent of the halo. The presence of the giant radio halo ( $\sim 1.2$  Mpc) in AS1063 therefore suggests a link to a cluster merger event. In line with the previous claims of an on-going merger by Gómez et al. (2012), Gruen et al. (2013).

#### 4.2. Curved radio spectra

The radio spectra of halos provide important information about the underlying particle (re-)acceleration mechanisms. According to the turbulent reacceleration model, we expect a cutoff in the energy spectrum of the CR electrons which also leads to a cutoff in the synchrotron emission above a certain frequency (e.g., Brunetti & Jones 2014). However, only a few clusters have been found that show this spectral steepening. Some examples are the Coma Cluster (Schlickeiser et al. 1987; Thierbach et al. 2003) and Abell 3562 (Giacintucci et al. 2005). A possible explanation for why very few clusters show spectral curvature are the observational difficulties involved. High quality flux density measurements at wide enough frequency spacing are hard to obtain. In addition, the magnetic field properties and amount of turbulence differ with location in the ICM. These inhomogeneous conditions result in spectra with different local cutoff frequencies. The spectral curvature is therefore less pronounced for the integrated spectra when these inhomogeneous conditions are present (e.g., ZuHone et al. 2013; Donnert et al. 2013; Pinzke et al. 2017).

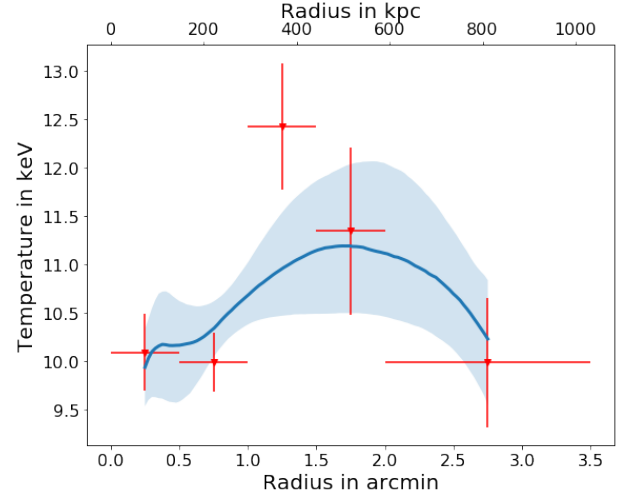


**Fig. 11.** Radial temperature profile of AS1063 obtained from *XMM-Newton* observations (Lovisari et al. in prep.). The size of the bins was set to be  $\geq 30''$  to limit the scatter of photons from bin to bin. The observed projected temperatures are shown by red points. The blue line and shaded area show the best-fit projected profile and its  $1\sigma$  uncertainty computed by using the best-fit three-dimensional model described in Vikhlinin et al. (2006).

Our flux density measurements of AS1063 show spectral steepening between 1.5 and 3 GHz, providing support for the turbulent reacceleration model. To characterize the spectral steepening, we compare our flux measurements to a Jaffe & Perola (JP, 1973) model with a “reasonable” injection spectral index of  $-0.8$  (Thierbach et al. 2003) in Figs. 4 and 10. A comparison with a JP model is useful here since a JP spectrum has a power-law shape with an exponential cutoff. The amount of spectral steepening for AS1063 is quite strong and well described by exponential cutoff. This would indicate that ICM conditions in AS1063 are rather homogeneous leading to similar cutoff frequencies at different spatial positions. For A370, the measurement uncertainties do not allow us to draw firm conclusions on the amount of spectral steepening.

It is important to stress that the observed spectral curvature for AS1063 is completely based on one measurement at 3 GHz. Therefore, future observations are important to confirm this result and characterize the shape of the radio spectrum in more detail.

## 5. Conclusions

In this paper, we presented 325 MHz GMRT and 1–4 GHz VLA observations of the Frontier Fields clusters AS1063 and A370. The results are summarized below:

1. We discovered a giant  $\sim 1.2$  Mpc radio halo in AS1063. The radio halo roughly follows the X-ray emission from the thermal ICM. We determined a radio halo power of  $P_{1.4\text{ GHz}} = (2.63 \pm 0.18) \times 10^{24} \text{ W Hz}^{-1}$ .
2. The integrated spectral index of the AS1063 radio halo measures  $-0.94 \pm 0.08$  between 0.325 and 1.5 GHz and it steepens to  $-1.77 \pm 0.20$  between 1.5 GHz and 3.0 GHz. This spectral steepening provides support for the turbulent reacceleration model for the formation of radio halos.
3. We discovered a faint radio halo in A370 with a size of about 500–700 kpc. The radio halo power is  $P_{1.4\text{ GHz}} = (2.00 \pm 0.16) \times 10^{24} \text{ W Hz}^{-1}$ . The radio halo is not detected at 3.0 GHz, with a  $3\sigma$  limit of 1.3 mJy. We measure a spectral index of  $-1.10 \pm 0.09$  between 0.325 and 1.5 GHz.

4. The radio halo powers of AS1063 and A370 follow the  $P_{1.4\text{GHz}} - Y_{500}$  scaling relation. Complementing our radio data with *Chandra* and *XMM-Newton* X-ray observations provides support for the idea that both radio halos are related to ongoing cluster merger events.

Future deep observations at both higher and lower frequencies will be important to better determine radio halo spectral shapes. We note that the relatively small spatial extent ( $3'$ ) and relatively high surface brightness of the AS1063 radio halo, make it a promising target for future observations with the VLA at 4–8 GHz and at  $\lesssim 1$  GHz with the uGMRT.

**Acknowledgements.** The National Radio Astronomy Observatory is a facility of the National Science Foundation operated under cooperative agreement by Associated Universities, Inc. We thank the staff of the GMRT that made these observations possible. GMRT is run by the National Centre for Radio Astrophysics of the Tata Institute of Fundamental Research. The scientific results reported in this article are based in part on observations made by data obtained from the *Chandra* Data Archive. Based on observations obtained with *XMM-Newton*, an ESA science mission with instruments and contributions directly funded by ESA Member States and NASA. RJW and AB acknowledge support from the VIDI research programme with project number 639.042.729, which is financed by the Netherlands Organisation for Scientific Research (NWO). LL acknowledges support from NASA through contracts 80NSSC19K0582 and 80NSSC19K0116. Basic research in radio astronomy at the Naval Research Laboratory is supported by 6.1 Base funding. This research made use of Astropy, (<http://www.astropy.org>) a community-developed core Python package for Astronomy (Astropy Collaboration 2013; 2018). This research made use of APLpy, an open-source plotting package for Python (Robitaille & Bressert 2012; Robitaille 2019).

## References

- Abell, G. O., Corwin, Jr., H. G., & Olowin, R. P. 1989, *ApJS*, **70**, 1  
 Ackermann, M., Ajello, M., Albert, A., et al. 2014, *ApJ*, **787**, 18  
 Ackermann, M., Ajello, M., Albert, A., et al. 2016, *ApJ*, **819**, 149  
 Arnaud, M., Pratt, G. W., Piffaretti, R., et al. 2010, *A&A*, **517**, A92  
 Astropy Collaboration (Robitaille, T. P., et al.) 2013, *A&A*, **558**, A33  
 Astropy Collaboration (Price-Whelan, A. M., et al.) 2018, *AJ*, **156**, 123  
 Basu, K. 2012, *MNRAS*, **421**, L112  
 Blasi, P., & Colafrancesco, S. 1999, *Astroparticle Physics*, **12**, 169  
 Bonafede, A., Giovannini, G., Feretti, L., Govoni, F., & Murgia, M. 2009, *A&A*, **494**, 429  
 Botteon, A., Gastaldello, F., & Brunetti, G. 2018, *MNRAS*, **476**, 5591  
 Briggs, D. S. 1995, Ph.D. Thesis, New Mexico Institute of Mining Technology,  
 Socorro, [www.atnf.csiro.au/people/tim.cornwell/research/danthesis.pdf](http://www.atnf.csiro.au/people/tim.cornwell/research/danthesis.pdf)  
 Broadhurst, T., Umetsu, K., Medezinski, E., Oguri, M., & Rephaeli, Y. 2008,  
*ApJ*, **685**, L9  
 Brown, S., & Rudnick, L. 2011, *MNRAS*, **412**, 2  
 Brunetti, G., & Jones, T. W. 2014, *Int. J. Mod. Phys. D*, **23**, 1430007  
 Brunetti, G., Setti, G., Feretti, L., & Giovannini, G. 2001, *MNRAS*, **320**, 365  
 Brunetti, G., Giacintucci, S., Cassano, R., et al. 2008, *Nature*, **455**, 944  
 Brunetti, G., Zimmer, S., & Zandanel, F. 2017, *MNRAS*, **472**, 1506  
 Cassano, R., Brunetti, G., & Setti, G. 2006, *MNRAS*, **369**, 1577  
 Cassano, R., Ettori, S., Brunetti, G., et al. 2013, *ApJ*, **777**, 141  
 Cassano, R., Ettori, S., Giacintucci, S., et al. 2010, *ApJ*, **721**, L82  
 Cornwell, T. J. 2008, *IEEE J. Sel. Top. Signal Process.*, **2**, 793  
 Cova, F., Gastaldello, F., Wik, D. R., et al. 2019, *A&A*, **628**, A83  
 Cuciti, V., Brunetti, G., van Weeren, R., et al. 2018, *A&A*, **609**, A61  
 Dennison, B. 1980, *ApJ*, **239**, L93  
 Donnert, J., Dolag, K., Brunetti, G., & Cassano, R. 2013, *MNRAS*, **429**, 3564  
 Feretti, L., Giovannini, G., Govoni, F., & Murgia, M. 2012, *A&ARv*, **20**, 54  
 Fujita, Y., & Ohira, Y. 2013, *MNRAS*, **428**, 599  
 Fujita, Y., Kohri, K., Yamazaki, R., & Kino, M. 2007, *ApJ*, **663**, L61  
 Giacintucci, S., Venturi, T., Brunetti, G., et al. 2005, *A&A*, **440**, 867  
 Giacintucci, S., Markevitch, M., Cassano, R., et al. 2017, *ApJ*, **841**, 71  
 Giacintucci, S., Markevitch, M., Cassano, R., et al. 2019, *ApJ*, **880**, 70  
 Giovannini, G., Feretti, L., Venturi, T., Kim, K. T., & Kronberg, P. P. 1993, *ApJ*, **406**, 399  
 Gómez, P. L., Valkonen, L. E., Romer, A. K., et al. 2012, *AJ*, **144**, 79  
 Govoni, F., Feretti, L., Giovannini, G., et al. 2001, *A&A*, **376**, 803  
 Govoni, F., Markevitch, M., Vikhlinin, A., et al. 2004, *ApJ*, **605**, 695  
 Gruen, D., Brimioule, F., Seitz, S., et al. 2013, *MNRAS*, **432**, 1455  
 Hart, Q. N., Stocke, J. T., & Hallman, E. J. 2009, *ApJ*, **705**, 854  
 Hoag, A. 1981, *Bull. Am. Astron. Soc.*, **13**, 799  
 Hoang, D. N., Shimwell, T. W., van Weeren, R. J., et al. 2019, *A&A*, **622**, A20  
 Intema, H. T. 2014, *Soc. India Conf. Ser.*, **13**  
 Intema, H. T., van der Tol, S., Cotton, W. D., et al. 2009, *A&A*, **501**, 1185  
 Intema, H. T., Jagannathan, P., Mooley, K. P., & Frail, D. A. 2017, *A&A*, **598**, A78  
 Jaffe, W. J., & Perola, G. C. 1973, *A&A*, **26**, 423  
 Kale, R., Shende, K. M., & Parekh, V. 2019, *MNRAS*, **486**, L80  
 Kale, R., Venturi, T., Giacintucci, S., et al. 2015, *A&A*, **579**, A92  
 Keshet, U., & Loeb, A. 2010, *ApJ*, **722**, 737  
 Kneib, J. P., Mellier, Y., Fort, B., & Mathez, G. 1993, *A&A*, **273**, 367  
 Lagattuta, D. J., Richard, J., Clément, B., et al. 2017, *MNRAS*, **469**, 3946  
 Lah, P., Pracy, M. B., Chengalur, J. N., et al. 2009, *MNRAS*, **399**, 1447  
 Liang, H., Hunstead, R. W., Birkinshaw, M., & Andreani, P. 2000, *ApJ*, **544**, 686  
 Lotz, J. M., Koekemoer, A., Coe, D., et al. 2017, *ApJ*, **837**, 97  
 Lovisari, L., & Reiprich, T. H. 2019, *MNRAS*, **483**, 540  
 Lovisari, L., Schindler, S., & Kapferer, W. 2011, *A&A*, **528**, A60  
 Lovisari, L., Forman, W. R., Jones, C., et al. 2017, *ApJ*, **846**, 51  
 Lynds, R., & Petrosian, V. 1986, *Bull. Am. Astron. Soc.*, **1014**  
 Martinez Aviles, G., Ferrari, C., Johnston-Hollitt, M., et al. 2016, *A&A*, **595**, A116  
 Mazzotta, P., & Giacintucci, S. 2008, *ApJ*, **675**, L9  
 McMullin, J. P., Waters, B., Schiebel, D., Young, W., & Golap, K. 2007, in  
 Astronomical Data Analysis Software and Systems XVI, eds. R. A. Shaw,  
 F. Hill, & D. J. Bell, *ASP Conf. Ser.*, **376**, 127  
 Mohan, N., & Rafferty, D. 2015, Astrophysics Source Code Library [record  
 ascl:1502.007]  
 Morandi, A., Ettori, S., & Moscardini, L. 2007, *MNRAS*, **379**, 518  
 Motl, P. M., Hallman, E. J., Burns, J. O., & Norman, M. L. 2005, *ApJ*, **623**, L63  
 Nagai, D. 2006, *ApJ*, **650**, 538  
 Offringa, A. R., de Bruyn, A. G., Biehl, M., et al. 2010, *MNRAS*, **405**, 155  
 Paczynski, B. 1987, *Nature*, **325**, 572  
 Pearce, C. J. J., van Weeren, R. J., Andrade-Santos, F., et al. 2017, *ApJ*, **845**, 81  
 Perley, R. A., & Butler, B. J. 2013, *ApJS*, **204**, 19  
 Petrosian, V. 2001, *ApJ*, **557**, 560  
 Pfrommer, C., & Enßlin, T. A. 2004, *A&A*, **413**, 17  
 Pinzke, A., Oh, S. P., & Pfrommer, C. 2017, *MNRAS*, **465**, 4800  
 Planck Collaboration XXVII. 2016, *A&A*, **594**, A27  
 Postman, M., Coe, D., Benítez, N., et al. 2012, *ApJS*, **199**, 25  
 Rajpurohit, K., Hoeft, M., van Weeren, R. J., et al. 2018, *ApJ*, **852**, 65  
 Rau, U., & Cornwell, T. J. 2011, *A&A*, **532**, A71  
 Richard, J., Kneib, J.-P., Limousin, M., Edge, A., & Jullo, E. 2010, *MNRAS*, **402**, L44  
 Robitaille, T. 2019, <https://doi.org/10.5281/zenodo.2567476>  
 Robitaille, T., & Bressert, E. 2012, Astrophysics Source Code Library [record  
 ascl:1208.017]  
 Savini, F., Bonafede, A., Brüggen, M., et al. 2019, *A&A*, **622**, A24  
 Scaife, A. M. M., & Heald, G. H. 2012, *MNRAS*, **423**, L30  
 Schlickeiser, R., Sievers, A., & Thiemann, H. 1987, *A&A*, **182**, 21  
 Sijbring, D., & de Bruyn, A. G. 1998, *A&A*, **331**, 901  
 Smail, I., Dressler, A., Kneib, J.-P., et al. 1996, *ApJ*, **469**, 508  
 Smail, I., Ivison, R. J., Owen, F. N., Blain, A. W., & Kneib, J.-P. 2000, *ApJ*, **528**, 612  
 Sommer, M. W., & Basu, K. 2014, *MNRAS*, **437**, 2163  
 Soucail, G., Fort, B., Mellier, Y., & Picat, J. P. 1987, *A&A*, **172**, L14  
 Strait, V., Bradač, M., Hoag, A., et al. 2018, *ApJ*, **868**, 129  
 Struble, M. F., & Rood, H. J. 1999, *ApJS*, **125**, 35  
 Thierbach, M., Klein, U., & Wielebinski, R. 2003, *A&A*, **397**, 53  
 Umetsu, K., Broadhurst, T., Zitrin, A., et al. 2011, *ApJ*, **738**, 41  
 van Weeren, R. J., Röttgering, H. J. A., Bagchi, J., et al. 2009, *A&A*, **506**, 1083  
 van Weeren, R. J., Brunetti, G., Brüggen, M., et al. 2016a, *ApJ*, **818**, 204  
 van Weeren, R. J., Ogrean, G. A., Jones, C., et al. 2016b, *ApJ*, **817**, 98  
 van Weeren, R. J., Ogrean, G. A., Jones, C., et al. 2017, *ApJ*, **835**, 197  
 van Weeren, R. J., Intema, H. T., Lal, D. V., et al. 2014, *ApJ*, **786**, L17  
 van Weeren, R. J., de Gasperin, F., Akamatsu, H., et al. 2019, *Space Sci. Rev.*, **215**, 16  
 Venturi, T., Giacintucci, S., Brunetti, G., et al. 2007, *A&A*, **463**, 937  
 Vikhlinin, A., Markevitch, M., Murray, S. S., et al. 2005, *ApJ*, **628**, 655  
 Vikhlinin, A., Kravtsov, A., Forman, W., et al. 2006, *ApJ*, **640**, 691  
 Williamson, R., Benson, B. A., High, F. W., et al. 2011, *ApJ*, **738**, 139  
 Wold, I. G. B., Owen, F. N., Wang, W.-H., Barger, A. J., & Keenan, R. C. 2012,  
*ApJS*, **202**, 2  
 ZuHone, J. A., Markevitch, M., Brunetti, G., & Giacintucci, S. 2013, *ApJ*, **762**, 78

## Appendix A: The spectral index uncertainty maps

Figures A.1 and A.2 show the uncertainty maps corresponding to the spectral index maps in Figs. 6 and 7, respectively. The

procedures to create the spectral index and uncertainty maps are explained in Sects. 2.4 and 2.3.

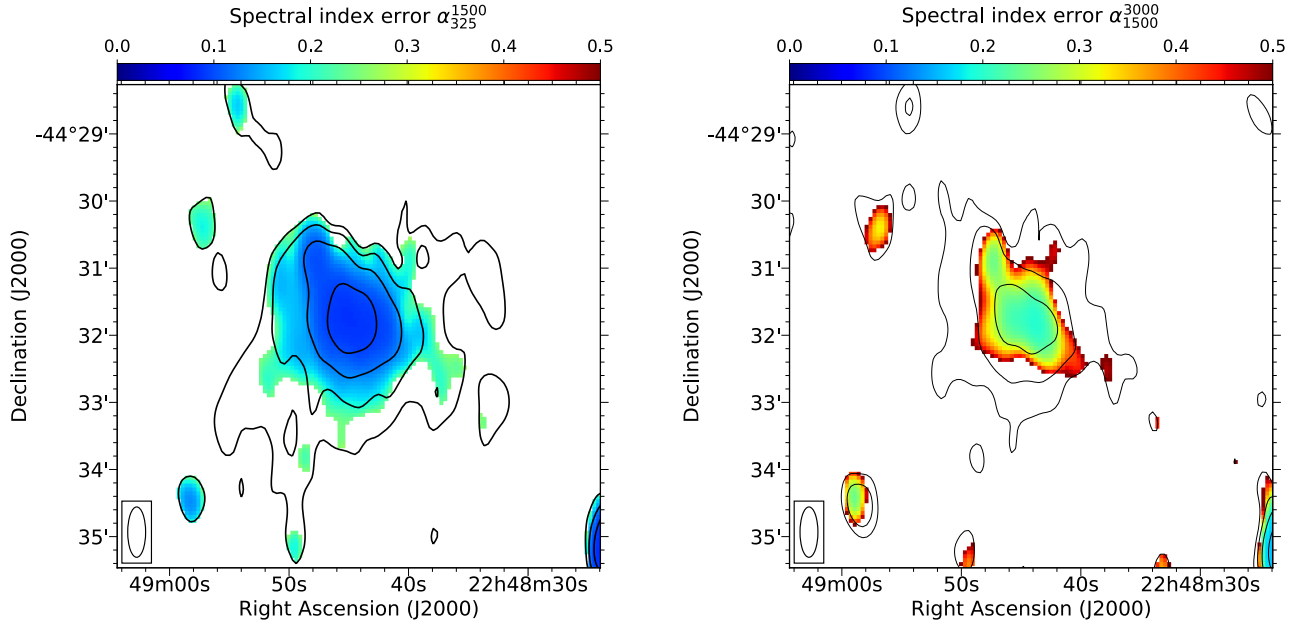


**Fig. A.1.** Spectral index uncertainty maps of AS1063 between 325 MHz and 1.5 GHz (left), and between 1.5 GHz and 3.0 GHz (right). The radio contours are from the 325 MHz (left) and 1.5 GHz (right) images and the same as shown in Fig. 6.

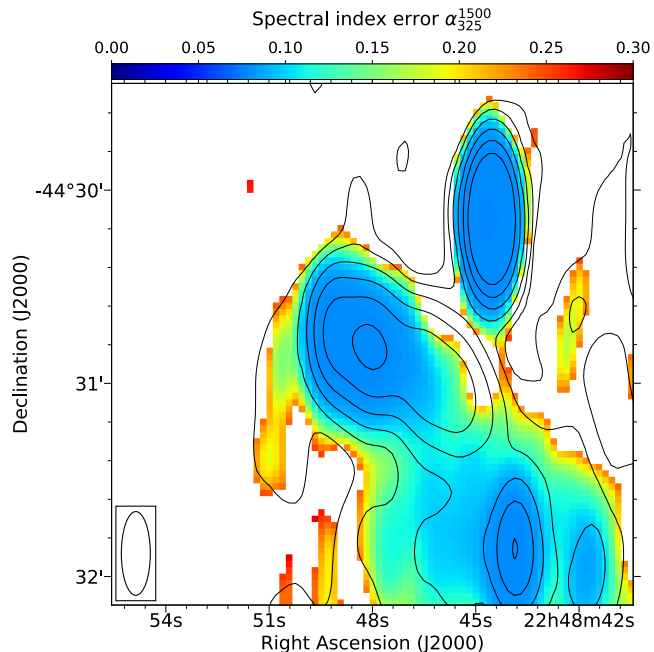


**Fig. A.2.** Spectral index uncertainty map of source D in AS1063 between 325 MHz and 1.5 GHz. The radio contours are from the 325 MHz image and the same as shown in Fig. 7.